Materials Advances

ROYAL SOCIETY OF CHEMISTRY

COMMUNICATION

View Article Online
View Journal | View Issue

Cite this: *Mater. Adv.*, 2023, 4, 6498

Received 11th August 2023,
Accepted 16th November 2023

DOI: 10.1039/d3ma00536d

rsc.li/materials-advances

Promising Ce single-atom-dispersed nitrogen-doped graphene catalysts for the hydrogen evolution reaction†

Sunny Yadav, Vandung Dao, Wenmeng Wang, Kai Chen, Chiyeop Kim, Gyu-Cheol Kim and In-Hwan Lee *

Single-atom (SA) anchored nitrogen-doped graphene (NGr) exhibits potential for efficient hydrogen production because of the advantages of maximum atomic utilization and surface-active energy. However, finding a suitable method for fabricating SA-containing catalysts with the desired metal loading without cluster formation is challenging. Here, well-dispersed Ce SAs on porous NGr catalysts were fabricated *via* a pyrolysis approach. 1Ce/NGr (1.0 wt% Ce) exhibited potential hydrogen evolution reaction (HER) performance in an alkaline medium: low onset overpotential and high stability, which was comparable to Pt/C (10.0 wt% Pt). The promising performance was attributed to the modification of the coordination environment and electronic structure between Ce SAs and the NGr host, which in turn serve as active sites for facilitating the adsorption and dissociation of water and liberating hydrogen molecules. This work offers new possibilities for designing rare-earth SA-based catalysts for water electrolysis.

Introduction

Hydrogen has become one of the most promising alternatives to depleting fossil fuels because of its renewability and clean energy production.[1] Therefore, hydrogen production as a fuel has become a global effort to create a sustainable power package for the future.[2,3] Hydrogen production through electrocatalytic water splitting has proven to be a substitute method for generating clean and sustainable fuel. Currently, only 4% of the world's hydrogen is generated *via* water splitting because the energy efficiency of water electrolysis is hindered by the reaction kinetics of the hydrogen evolution reaction (HER) owing to high overpotentials.[4] The design of efficient catalysts is crucial for minimizing the overpotential and improving the energy efficiency of the HER.[2] Unfortunately, existing catalysts still have a significant gap in their HER performance, preventing the complete substitution of Pt. Poor catalytic performance occurs in catalytic redox reactions because of the limited availability of active sites. For example, only the outer surface metal atoms are primarily used in nanomaterials, while the inner atoms remain uninvolved.[5] Single-atom catalysts (SACs) have been reported as efficient electrocatalysts for the HER because of their maximum atomic utilization, high activity, selectivity, and stability.[6,7] However, preparing SACs without aggregation is quite challenging because of their high surface energy. Consequently, the metal loading is usually kept low, which results in a low number of active sites and affects catalytic activity. Generally, it is challenging to find a suitable method for preparing SACs with the desired metal dispersion density to improve their overall catalytic performance for the HER. Unfortunately, until now, no efforts have been made to synthesize rare-earth element SACs (REE-SACs) for electrochemical purposes. Considering these limitations, we became interested in developing new stable REE-SACs that can sufficiently anchor single atoms to prevent aggregation and yield high catalytic activity.

Thus far, metal N-doped carbon SACs have played the most vital role in electrocatalysis.[5,8,9] Utilizing REE-SACs as potential materials for electrocatalysis can be a crucial research direction since REEs provide distinctive electronic structures due to the spin–orbit coupling of their 4f and valence orbitals.[10,11] Among REEs, Ce stands out because of its rich electronic orbital configuration, which includes unique 4f orbitals that exhibit complex chemical states with variable oxidation states and coordination numbers. The electronic communication between Ce^{3+} and Ce^{4+} oxidation states allows Ce to generate defects by losing electrons, which can serve as active catalytic sites and modify the coordination environment and electronic structure of neighboring atoms, thus enhancing catalytic processes.[11–15] Ce displays a wide range of valence states from 0 to +4 and exhibits excellent stability in alkaline environments. In alkaline

Department of Materials Science and Engineering, Korea University, Seoul 02841, Republic of Korea. E-mail: ihlee@korea.ac.kr

† Electronic supplementary information (ESI) available. See DOI: https://doi.org/10.1039/d3ma00536d

electrolytes, the HER occurs through mechanisms such as the Volmer–Heyrovsky mechanism, [$H_2O + e^- \rightarrow H_{ad} + OH^-$] and [$H_{ad} + H_2O + e^- \rightarrow H_2 + OH^-$], or the Volmer–Tafel mechanism, [$H_2O + e^- \rightarrow H_{ad} + OH^-$] and [$2H_{ad} \rightarrow H_2$].[16–18]

The introduction of Ce can enhance water adsorption and dissociation because of its high binding energy, which decreases the energy barrier of the reaction and increases the reaction rates.[19] Considering these practical predictions, we assume Ce single-atom-based electrocatalysts can effectively catalyze the HER. The uniform dispersion of single atoms requires an ultrathin high surface area that allows for high mass loading and electron transport between catalytic centers. Graphene can be tuned with heteroatoms, such as N, to create additional defective sites because it activates the adjacent C atoms, thereby creating novel sites that anchor the single atoms for improved electrocatalytic reactions.[20,21] Since nitrogen has a high electronegativity, NGr can prevent catalyst agglomeration and provide a conducive environment for an efficient HER by generating additional active sites for the adsorption of reactants caused by the polarization effect.[22–27] The unique electronic and structural properties of Ce and NGr can interact synergistically to improve catalytic activity, stability, and selectivity, thereby contributing to the excellent HER performance of Ce-based electrocatalysts.

Herein, we describe a novel strategy for developing porous catalysts by exposing additional active sites and enhancing mass transport, both of which result in increased catalytic activity. This strategy can be used to modulate the dispersion of Ce single atoms on NGr efficiently. The key to synthesizing Ce-based SACs is to effectively maximize the interaction between Ce atoms and the NGr support to prevent the Ce atoms from aggregating during pyrolysis. Moreover, we discovered that Ce single atoms supported on NGr (Ce/NGr) exhibit remarkable catalytic performance for the electrocatalytic HER because of the atomically dispersed Ce active sites. To understand the nature of the active sites, the obtained catalysts were comprehensively characterized, and Ce/NGr was found to exhibit long-term stability at −0.35, −0.7, and −1.0 V *vs.* a reversible hydrogen electrode (RHE), which is higher than that of NGr. Long-term current *versus* time (*I*–*t*) tests revealed the excellent stability of atomically dispersed Ce/NGr. At the same time, the aberration-corrected high-angle annular dark-field scanning transmission electron microscopy (HAADF-STEM) images and X-ray photoelectron spectroscopy (XPS) data demonstrated that Ce was atomically dispersed in NGr. Developing a strategy for synthesizing SACs with a tunable metal-loading content and understanding the critical role of rare-earth Ce single atoms in the performance of the electrocatalytic HER offer new opportunities for the scientific cognition and application of REE-SACs. The physical state of the active sites has been linked with the 'performance of the catalyst and the selectivity of the aqueous electrolyte. Thus, a three-electrode system was used to compare the physical state of the active catalyst. To access the activity of the catalyst, linear sweep voltammetry (LSV) was used to extract the onset potential, exchange current density, and limiting current.

Results and discussion

Preparation and characterization techniques

Fig. S1 (ESI†) presents the efficient route for synthesizing rare-earth Ce single atoms dispersed in NGr using a pyrolysis method. First, the C precursor (glucose), N precursor (dicyanamide), and the metal precursor were mixed in a solution containing a sacrificial silica support. The obtained solution was freeze-dried to remove distilled water (DI) completely. Subsequently, the resultant powder was pyrolyzed in an inert atmosphere to disperse the isolated Ce single atom on NGr. The final samples for subsequent characterization and electrochemical tests were obtained by further grinding the as-obtained pyrolyzed samples. After pyrolysis, the silica was dissolved, leaving behind a porous carbon network with active Ce sites. In this synthetic strategy, the freeze-drying stage can further contribute to a high surface area after pyrolysis. To demonstrate the impressive HER capabilities of Ce/NGr, which arise from the dispersion of Ce atoms on the porous surface of NGr, we prepared two variants: 1Ce/NGr containing 1.0 wt% Ce and 3Ce/NGr containing 3.0 wt% Ce.

The morphology and design of a catalyst can significantly enhance its electrochemical performance. Fig. 1a and b shows the field-emission scanning electron microscopy (FE-SEM) images of NGr and Ce/NGr. The SEM image shows that NGr exhibited a multilayer, sheet-like, and highly wrinkled structure (Fig. 1a), which is believed to have increased the surface area of the nanosheets and offered them unique conductivity and catalytic properties that improved the electrochemical performance. The energy-dispersive X-ray spectroscopy (EDS) elemental mapping for NGr (Fig. S2, ESI†) and Ce/NGr (Fig. S3, ESI†) is also provided. Meanwhile, an amorphous structure can also be observed, indicating that numerous defects were formed owing to the presence of Ce atoms.[28] Notably, pores were detected on the NGr and Ce/NGr surfaces after silica etching (Fig. 1b), indicating the formation of hierarchically macro–meso–microporous NGr, which acts as a trap for Ce single atoms and consequently aids in enhancing mass transport and catalytic activity. The as-pyrolyzed Ce/NGr morphology was further analyzed using high-resolution transmission electron microscopy (HR-TEM). Uniform and multilayered structures were observed, indicating that the N and Ce atoms were incorporated into the graphene network, as shown in Fig. S4a (ESI†). Additionally, wrinkles were detected in NGr and Ce/NGr in each basic unit. Fig. S4a–d (ESI†) shows the TEM images of free-standing NGr, NGr with silica doping, silica covered with NGr, and NGr after silica removal, respectively. No noticeable Ce atoms were detected through bright-field TEM observation. High-magnification HAADF-STEM measurements were performed to confirm further the homogenous dispersion of the Ce atoms within the NGr support. Here, we successfully constructed atomically dispersed Ce sites that were embedded in a hierarchically macro–meso–microporous N-doped carbon catalyst. As shown in Fig. 1c and e, isolated bright spots can be clearly distinguished from the matrix, suggesting that the Ce atoms were atomically dispersed in NGr. Further observation of the HAADF-STEM images of Ce/NGr reveals

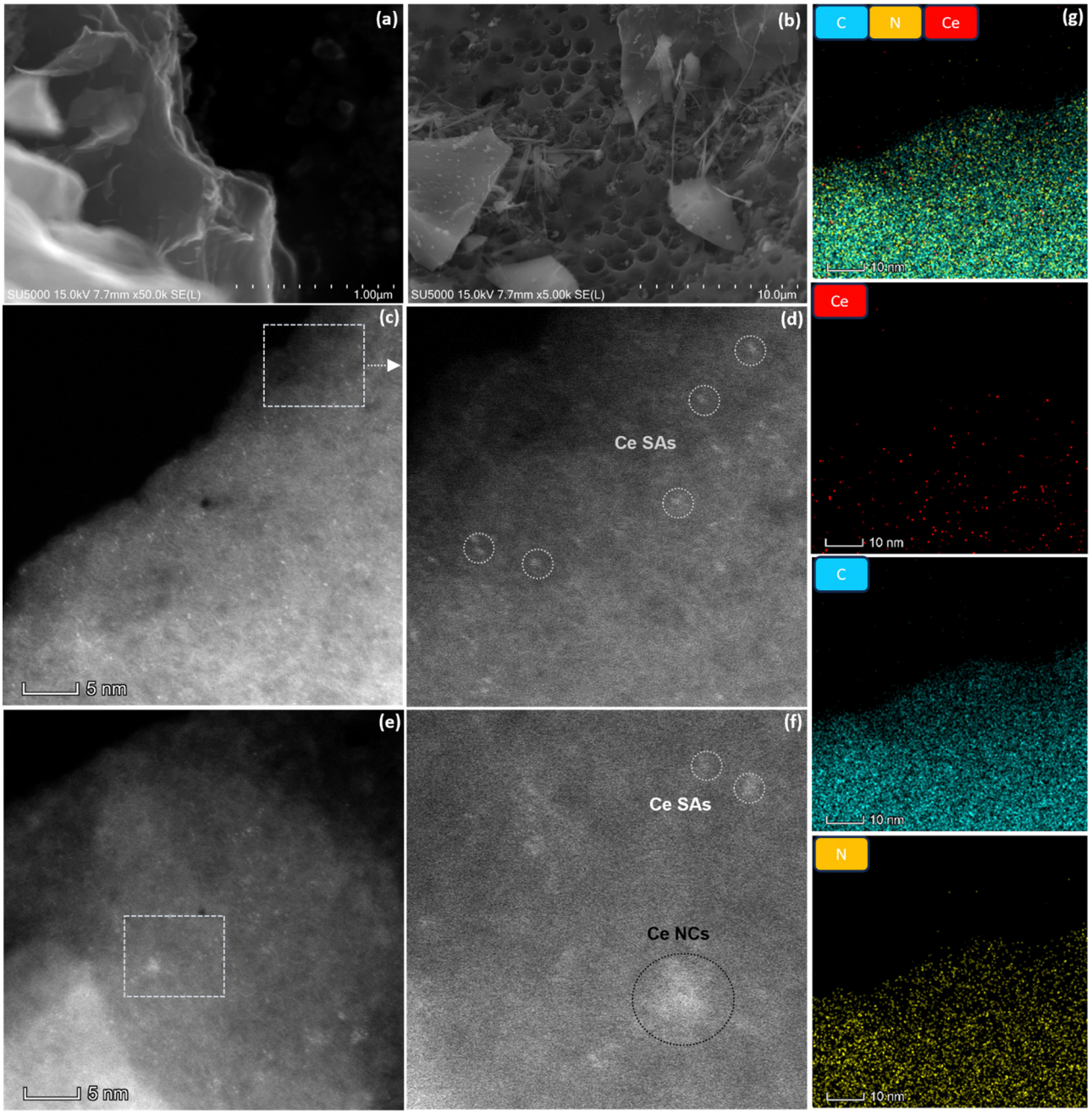

Fig. 1 (a) FE-SEM images showing the multilayered and wrinkled structure of NGr, (b) porous structure of Ce/NGr after silica etching, (c) and (d) aberration-corrected HAADF-STEM image for 1Ce/NGr, (e) and (f) 3Ce/NGr, and (g) elemental mapping of Ce, C and N.

high-density bright spots (Fig. 1c and d) with no noticeable agglomeration up to a certain low atomic weight percent. Nevertheless, Ce aggregates can easily develop during pyrolysis if the Ce precursor is increased. Noteworthily, the images obtained for 3Ce/NGr depict the presence of densely distributed single atoms on the substrate without any significant agglomeration (Fig. S5, ESI†). Additionally, 3Ce/NGr mainly comprised Ce single atoms without large nanoclusters due to 'dispersion of Ce *via* the freeze-drying approach (Fig. 1e, f, and Fig. S6, ESI†). The EDS mapping (Fig. 1g) shows that the Ce, C, and N atoms were evenly distributed in the entire framework. Fig. 2a shows the X-ray diffraction (XRD) data for the atomically dispersed NGr and Ce/NGr catalysts. All the samples exhibit two broad shoulder peaks at 23° and 43°, which are indexed to the (002) and (010) stackings of NGr, respectively.[29–31] Moreover, there are no characteristic metal peaks that reflect the presence of Ce species, suggesting that the Ce atoms were highly dispersed in the prepared samples, as shown in the elemental mapping images of Ce/NGr. Raman spectroscopy was performed to extract structural information for NGr and Ce/NGr (Fig. 2b). The details collected from the different samples revealed characteristic D and G bands at peaks located at 1370 cm^{-1} and 1590 cm^{-1},[32,33] and the I_D/I_G ratios of NGr and Ce/

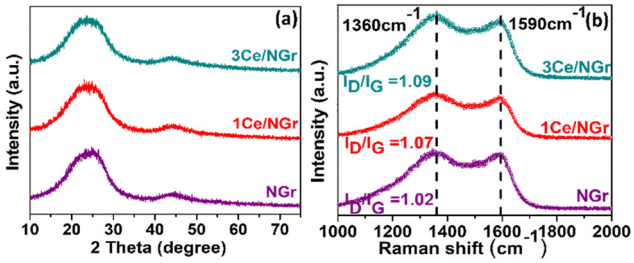

Fig. 2 (a) XRD patterns and (b) Raman spectra for NGr, 1Ce/NGr and 3Ce/NGr.

NGr were 1.02 and 1.06, respectively. The higher I_D/I_G ratio of Ce/NGr indicates that additional defects were created within the N-doped species, resulting in the presence of more active sites. All the samples exhibited the same ordered carbon structure regardless of morphology and Ce doping content. Studies have shown that the presence of both defective carbon and graphitized carbon plays a significant role in improving electrochemical performance by fine-tuning the local electronic and geometric characteristics of the carbon matrix.[5] XPS was performed to quantitatively analyze the chemical compositions of the as-prepared materials (C, N, and Ce). Here, C, N, and Ce were detected in Ce/NGr, which is consistent with the elemental mapping results. Fig. 3a shows the XPS complete survey. The high-resolution C 1s spectra revealed the bonding state for the C atom present in the NGr support, as shown in Fig. 3b. The main peak for NGr corresponds to sp^2 C–C (284.45 eV), C–N (285.45 eV), and C═N (288.81 eV).[3,33,34] The high-resolution N 1s spectra (Fig. 3c) exhibit four main peaks at 397.82 eV, 399.37 eV, 400.48 eV, and 401.80 eV, indicating the coexistence of pyridinic N, pyrrolic N, graphitic N, and quaternary N, respectively.[3,34–39] The Ce–N bond (398.2 eV) can be found in the high-resolution N 1s XPS spectrum of Ce–N (Fig. 3d).[40,41] Using pyrolysis to create NGr results in the formation of an sp^2 bond in the carbon structure, which can strongly affect the fast electron-transfer kinetics influenced by metal doping during pyrolysis.[42] Previous research has demonstrated that doping single metal atoms into a C matrix induces a high pyridinic N content. Relatively, we believe that the high percentage of pyridinic N in Ce/NGr suggests the presence of abundant atomic Ce–N moieties. The Ce 3d peaks were obtained around 905–885 eV, which were assigned to Ce^{3+} $3d_{5/2}$ and $3d_{3/2}$, respectively, suggesting that the nature of Ce is ionic Ce^{3+}. Owing to the small concentration of Ce in 1Ce/NGr (Fig. 3e), the XPS intensity of Ce^{3+} was not clear, but as the concentration increased to 3Ce/NGr, the peak intensity became clear (Fig. 3f).[43–47]

Electrocatalytic investigations

The electrocatalytic HER performance was evaluated at 25 °C using a Biologic VSP-300 science instrument with a standard three-electrode system. A platinum wire and Hg/HgO were used as the counter and reference electrodes, respectively, for the HER. The active catalyst coated with Ni foam (1 cm × 1 cm) was employed as the working electrode. The potentials were converted into RHE using the following equation:

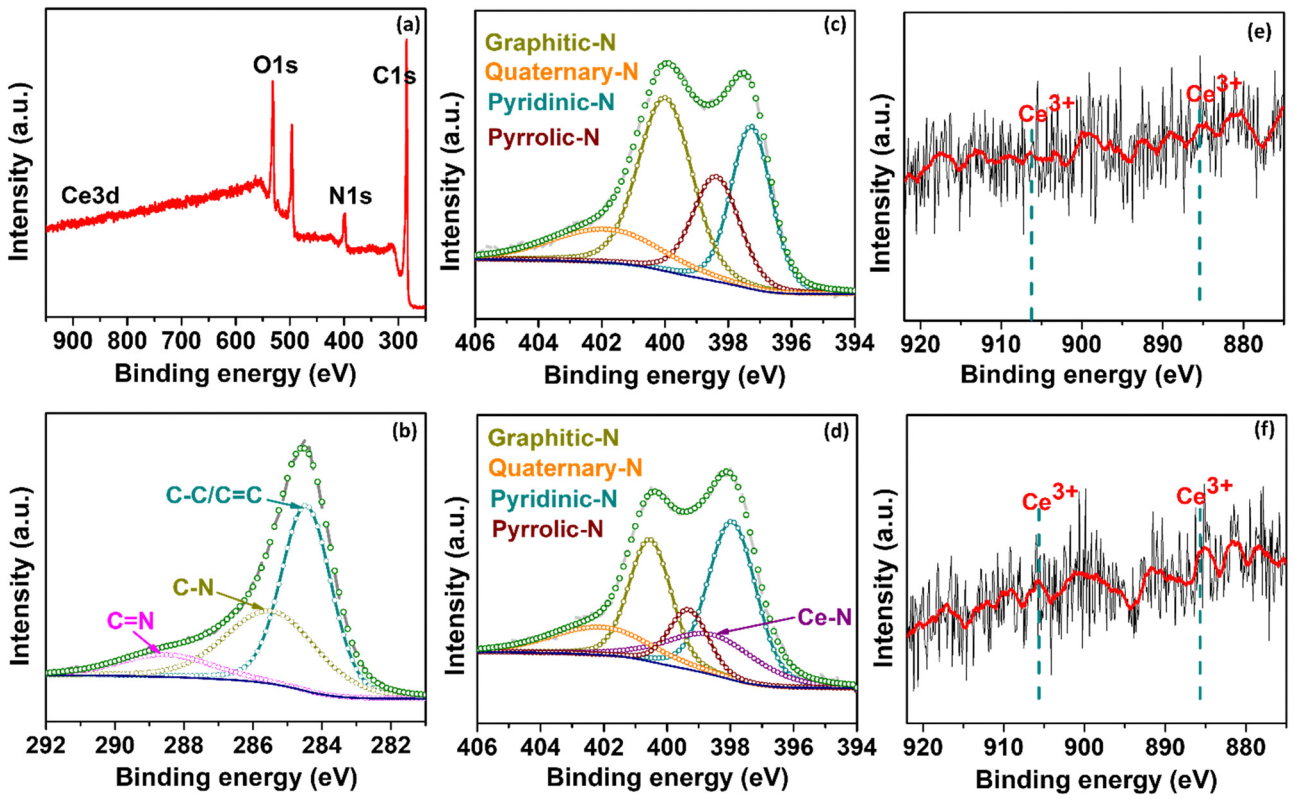

Fig. 3 (a) Full survey spectra for 1 Ce/NGr, (b) C 1s for NGr, (c) N 1s for NGr, (d) N 1s for 1Ce/NGr, (e) Ce^{3+} for 1Ce/NGr, and (f) Ce^{3+} for 3Ce/NGr.

$$E(vs.\ \text{RHE}) = E(vs.\ \text{Hg/HgO}) + 0.198 + 0.059\ \text{pH}.$$

5 mg of the catalyst was added to 950 μL of ethanol and 50 μL of Nafion to prepare the working electrode. The resulting solution was ultrasonicated for 1 h to form a homogenous catalyst slurry. The slurry was drop-cast onto Ni foam and dried under ambient conditions. All measurements were conducted in a 1 M potassium hydroxide (KOH) solution. The polarization curve was measured using the LSV technique at 5 mV s^{-1} with a 90% *IR* correction and an automatic impedance method performed using a BioLogic instrument. Electrochemical impedance spectroscopy (EIS) was performed at an overpotential of 10 mV in the frequency range of 200 kHz to 100 mHz. The double-layer capacitance (C_{dl}) was determined by plotting ΔJ (J_a–J_c) *vs.* different scan rates using cyclic voltammetry (CV) in the nonredox potential window of 0–0.2 V *vs.* Hg/HgO in 1 M KOH. The measured slope value was twice the C_{dl}.

Electrochemical measurements

The HER activity of the Ni foam, Pt/C, NGr, 1Ce/NGr, and 3Ce/NGr was evaluated using a three-electrode electrochemical cell in an alkaline medium. The catalyst loading on the electrode was displayed in the linear sweep voltammograms at a scan rate of 5 mV s^{-1} in 1 M KOH after a 90% IR compensation. Commercial Pt/C with the same mass loading was also included as a reference point. As expected, Pt/C exhibited enhanced HER catalytic activity (Fig. S7a, ESI†). Fig. 4a shows the HER polarization curve of the Ni foam, Pt/C, NGr, 1Ce/NGr, and 3Ce/NGr in 1 M KOH. The results revealed that the best HER electrocatalytic performance was exhibited by the 1Ce/NGr catalyst,

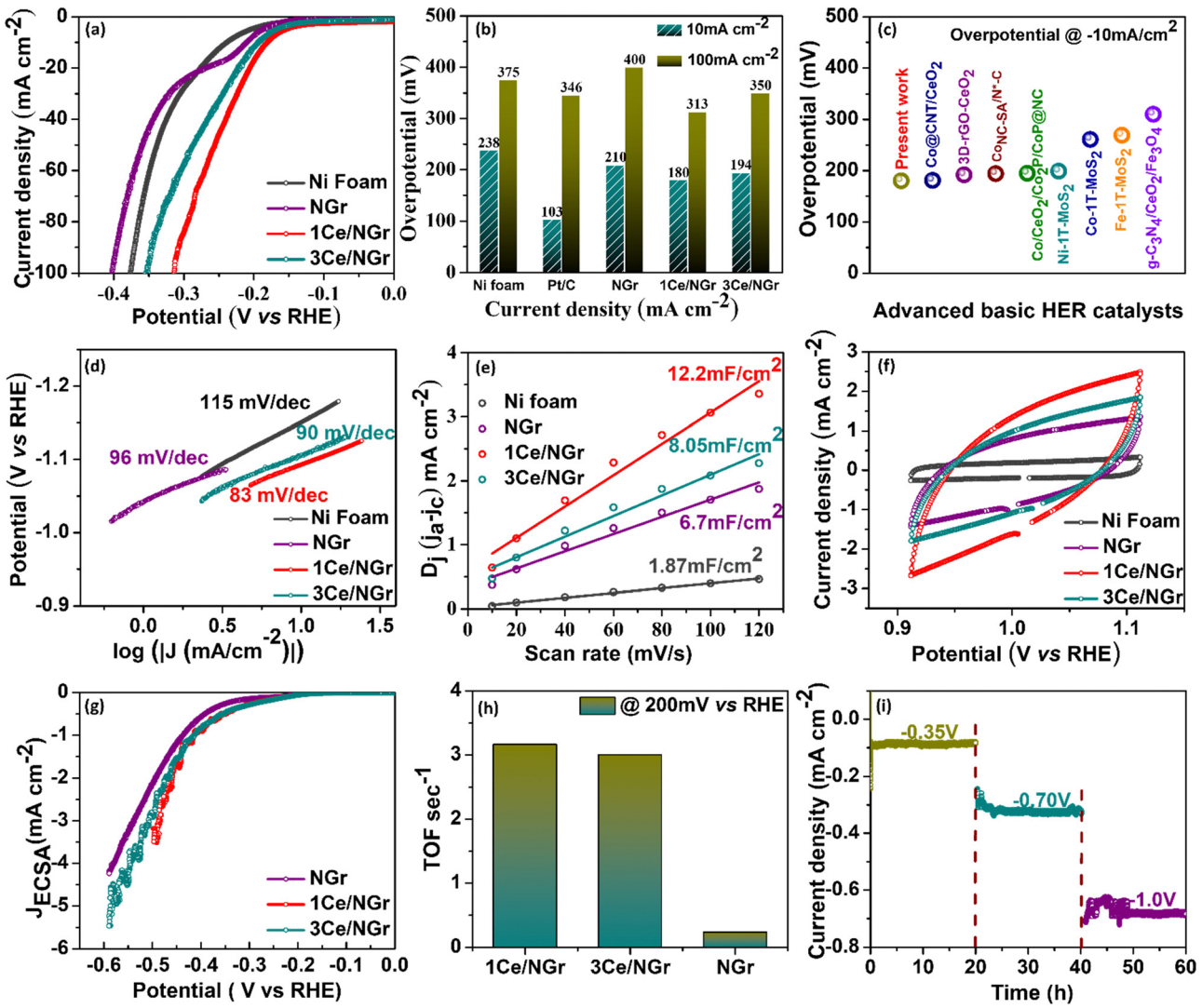

Fig. 4 (a) HER polarization curves for Ni foam, NGr, 1Ce/NGr, and 3Ce/NGr; (b) HER overpotentials for Ni foam, Pt/C, NGr, 1Ce/NGr, and 3Ce/NGr at a current density of 10 and 100 mA cm^{-2}; (c) comparison of the prepared catalyst and other previously reported catalysts at a constant overpotential of 10 mA cm^{-2}; (d) Tafel plot of Ni foam, NGr, 1Ce/NGr, and 3Ce/NGr; (e) extraction of the double layer capacitance (C_{dl}) of Ni foam, NGr, 1Ce/NGr, and 3Ce/NGr; (f) CV cycle of Ni foam, NGr, 1Ce/NGr and 3Ce/NGr at 100 mV s^{-1}; (g) ECSA-normalized LSV polarization curve of NGr, 1Ce/NGr, and 3Ce/NGr; (h) calculated TOF values of NGr, 1Ce/NGr, and 3Ce/NG at 200 mV *vs.* RHE; (i) *I*–*t* graph of 1Ce/NGr at different potentials.

which required a lower onset potential (~180 mV) than 3Ce/NGr (194 mV), NGr (210 mV), and the Ni foam (238 mV) which is comparable with Pt/C (103 mV). Moreover, 1Ce/NGr achieved a current density of −100 mA cm^{-2} at a potential of −313 mV as opposed to NGr, which required a higher potential to reach the same current density. Fig. 4b shows the overpotentials of these catalysts at current densities of 10 and 100 mA cm^{-2}. The results demonstrate that abundant active sites were present in Ce/NGr, which strengthened the HER activity of the catalyst. Fig. 4c compares the prepared catalyst and other previously reported catalysts at a constant overpotential of 10 mA cm^{-2} listed in Table S1 (ESI†). The image revealed that the voltage achieved by the prepared catalyst was significantly lower than those of previously reported catalysts. Fig. 4d shows that 1Ce/NGr had a lower calculated Tafel slope (83 mV dec^{-1}) than Ni foam (115 mV dec^{-1}), NGr (96 mV dec^{-1}), and 3Ce/NGr (89 mV dec^{-1}).[48] This suggests that the engineered defect-rich Ce-based SACs can achieve high reaction rates and fast kinetics for water splitting. The Nyquist plots obtained from the EIS analysis of the products revealed that 1Ce/NGr had a remarkably lower charge-transfer resistance (R_{ct}) of 0. 677 Ω than NGr (3.121 Ω) and 3Ce/NGr (1.835 Ω), indicating an expeditious charge transfer (Fig. S7c, ESI†). The significant reduction in the R_{ct} values can be attributed to the rapid electron-transfer kinetics between Ce and NGr, which can be attributed to the increased number of active sites and improved conductivity of NGr. The unobstructed redox shift from Ce^{3+} to Ce^{4+} could improve the ionic/electronic conductivity and reduce the R_{ct}.[49,50] The electrochemical surface area (ECSA) was estimated using the C_{dl} under the CV curves to further probe the intrinsic activity of the electrocatalysts (Fig. 4e and f). Furthermore, 1Ce/NGr had a larger C_{dl} value of 12.2 mF cm^{-2} than the Ni foam (1.87 mF cm^{-2}), NGr (6.7 mF cm^{-2}), and 3Ce/NGr (8.05 mF cm^{-2}). Therefore, it was determined that 1Ce/NGr had a larger ECSA value (305 cm^2) than Ni foam (46.7 cm^2), NGr (167.50 cm^2), and 3Ce/NGr (201.3 cm^2). Fig. S8 (ESI†) shows further CV plots of Pt/C, the Ni foam, NGr, 1Ce/NGr, and 3Ce/NGr at different scan rates. To further evaluate the metal utilization efficiencies and access the intrinsic activities of catalysts, their specific activities, mass activities, and TOFs were calculated. In order to assess the performance of the catalysts based on their surface characteristics, the LSV data were normalized by the ECSA to determine the intrinsic HER activity (Fig. 4g). Normalization of the current by the ECSA demonstrates that 1Ce/NGr displayed the lowest potential, indicating that the active sites in 1Ce/NGr possess higher inherent activity, followed by 3Ce/NGr and NGr. Through a comparison of the ECSA-normalized activities (Fig. 4g),[51–53] it is evident that 1Ce/NGr still serves as the state-of-the-art catalyst in electrolysis with a relatively small η_3 of −494 mV, followed by 3Ce/NGr and NGr having an overpotential of 525 mV and 561 mV. For comparison, the mass activity graph for Pt/C and 1Ce/NGr is also shown in Fig. S7b (ESI†). While the overpotential of catalysts has relevance to their device applicability, TOFs can reveal an intrinsic catalytic activity of Ce single atoms present as active sites over the NGr surface. Among the compared catalysts, 1Ce/NGr catalysts showed the highest activity, with a TOF of 3.16 s^{-1}, 3 s^{-1}, and 0.238 s^{-1} at an overpotential of 200 mV, confirming the higher effect of Ce single atom sites (Fig. 4h).[54] Generally, long-term stability is also an important parameter for analyzing the electrochemical properties of catalysts (Fig. 4i and Fig. S9a, b, ESI†). Notably, 1Ce/NGr demonstrated a robust and steady current density at voltages of −0.35 V, −0.7 V, and −1.0 V for 60 h, indicating that it exhibits excellent stability (Fig. 4i). For comparison, we carried out the electrochemical measurement using another counter electrode, *i.e.*, graphite electrode, and the results are provided in Fig. S10 and S11 (ESI†). The results depict that the engineered defect-rich Ce-based SACs show better electrochemical activity. Fig. S10a (ESI†) presents the HER polarization curve of the Ni foam, NGr, 1Ce/NGr, and 3Ce/NGr in 1 M KOH. The results revealed that the best HER electrocatalytic performance was exhibited by the 1Ce/NGr catalyst, which required a lower onset potential (197 mV) than 3Ce/NGr (217 mV), NGr (223 mV), and the Ni foam (238 mV). Fig. S10b (ESI†) shows that 1Ce/NGr had a lower calculated Tafel slope (88 mV dec^{-1}) than Ni foam (113 mV dec^{-1}), NGr (96 mV dec^{-1}), and 3Ce/NGr (92 mV dec^{-1}), suggesting the high reaction rates and fast kinetics of the defect-rich Ce-based SACs. Furthermore, the C_{dl} was determined by using CV in the nonredox potential window, and we found out that 1Ce/NGr had a larger C_{dl} value of 9.99 mF cm^{-2} than the Ni foam (2.69 mF cm^{-2}), NGr (2.97 mF cm^{-2}), and 3Ce/NGr (4.97 mF cm^{-2}) (Fig. S10c, ESI†). Therefore, it was determined that 1Ce/NGr had a larger ECSA value (249.75 cm^2) than Ni foam (67.25 cm^2), NGr (74.25 cm^2), and 3Ce/NGr (124.25 cm^2) (Fig. S10d, ESI†). Fig. S11 (ESI†) shows further CV plots of Pt/C, the Ni foam, NGr, 1Ce/NGr, and 3Ce/NGr at different scan rates. The results clearly depict that the engineered defect-rich Ce-based SACs show better electrochemical activity. Still, we believe that the instability of the graphite rod leads to the degradation of the carbon species, resulting in coverage of active sites and thus high overpotential. The results clearly show that using a Pt counter electrode over a graphite electrode benefits our work. For this reason, we still used Pt mesh as the counter electrode in this work.

The isolated Ce metal atoms supported on porous NGr show definite geometric configuration and electronic structure, which are beneficial for the exploration of the reaction mechanism. To gain further insights into the reaction mechanism of the catalyst for the HER, after the long-term stability test, the changes in the morphology, structure, and chemical state of Ce/NGr were characterized using SEM, HAADF-STEM, and XPS. The SEM results show (Fig. S12a, b and S13, ESI†) that, after testing the obtained samples for a long time, the porous structure maintains good structural stability. Also, the EDS spectra of NGr (Fig. S14, ESI†) and Ce/NGr (Fig. S15, ESI†) after the stability test are shown. The Cs-TEM images obtained after testing show the presence of bright spots, demonstrating that Ce exists in Ce/NGr in the form of single atoms (Fig. S12c and d, ESI†). The elemental mapping showing the presence of Ce is also shown in Fig. S12e (ESI†). XPS analysis was employed to characterize the shifts in the chemical states to further analyze

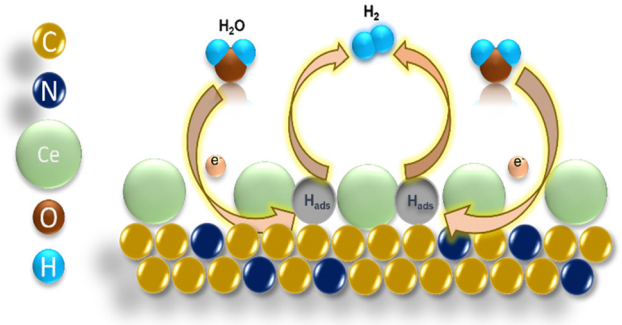

Fig. 5 Possible mechanism for HER activity in an alkaline medium over the Ce/NGr catalyst.

the changes in the electronic structure of the obtained Ce/NGr samples before and after the stability test. Fig. S12f–h (ESI†) shows the distribution of N 1s and Ce atoms after deconvolution. The results obtained for N 1s are consistent with the N 1s of Ce/NGr before the HER, showing minor shifts in the peaks. We found the peaks of Ce^{4+} after the stability test, indicating that Ce^{3+} lost electrons during the HER process and formed Ce^{4+}, indicating that Ce can significantly regulate the electronic state and structure of the electrocatalyst, thus accelerating the electrochemical HER performance. Based on the above results, we propose an HER mechanism for the Ce single atoms in the alkaline electrolyte. The specific reaction mechanism involving two steps is as follows: (1) Volmer step (eqn (1)): a water molecule diffuses to an active Ce site, where it is absorbed and dissociated into an OH* and H_{ads}. The H_{ads} species preferentially combine with Ce atoms nearby because of its high binding energy, which decreases the energy barrier of the reaction and increases the reaction rates. (2) The Heyrovsky step (eqn (2)): as the water-dissociation reaction proceeds, a great many H_{ads} species are generated, which can later combine with other H_{ads} species to form H_2 molecules, and the resulting H_2 gas is released from the surface of NGr. We believe that, during the HER, the Ce active site could start the reaction mechanism by losing electrons, thus reducing the energy barrier in the reaction pathway, and the corresponding electronic interaction between the catalysts is shown in the schematic representation in Fig. 5.

$$[H_2O + e^- \rightarrow Ce\text{–}H_{ad} + OH^-]\ Ce^{3+} \quad (1)$$

$$[Ce\text{–}H_{ad} + H_2O + e^- \rightarrow H_2 + OH^-]NGr \quad (2)$$

Conclusions

In this study, a porous catalyst was successfully developed for the electrocatalytic HER by controlling the dispersion of Ce single atoms in NGr using a pyrolysis method. The controlled dispersion of Ce single atoms in NGr maximizes atomic utilization and provides surface-active energy, leading to improved catalytic performance. The Ce/NGr catalyst exhibited a remarkable catalytic performance with a lower onset potential, a higher current density, and faster charge-transfer kinetics than the other catalysts, such as Ni foam and NGr. The catalyst also demonstrated good stability over long-term testing, as evidenced by its sustained and steady current densities over a 60-hour testing period. This remarkable stability is attributed to the robust interaction between the Ce single atoms and the NGr support, which prevents aggregation and maintains high catalytic activity. The characterization results confirmed the atomic dispersion of Ce in NGr and the presence of hierarchically macro–meso–microporous structures, which contributed to increased mass transport and catalytic activity. The results suggest that the engineered Ce/NGr catalyst has great potential for efficient water electrolysis and provides new opportunities for designing and tuning electrocatalysts at the atomic level for efficient water electrolysis.

Experimental section

Chemicals

All the chemicals used in this study were used as received without further purification. Cerium(III) nitrate hexahydrate (99.99%), glucose (99.5%), dicyandiamide (99.0%), tetraethyl orthosilicate (TEOS), and 5 wt% Nafion solutions were purchased from Sigma-Aldrich. Additionally, 1 M KOH, ethyl alcohol (99.5%), and an ammonia solution (25.0–30%) were obtained from Samchun. Sodium hydroxide was obtained from Daejung.

Silicon dioxide synthesis

To synthesize silicon dioxide (SiO_2), 80 mL of ethanol and 19 mL of DI water were added to a beaker and stirred for 10 min. Thereafter, 5 mL of the ammonia solution was added to the mixture, which was then stirred for 30 min. Subsequently, the SiO_2 precursor, TEOS, was added to the ammonium–alcohol solution. The reaction was allowed to proceed at room temperature under continuous stirring for 1 h. After the reaction period, the SiO_2 particles were cleaned by repeatedly washing and centrifuging with DI water. Finally, the SiO_2 nanoparticles were dispersed in 5 mL of DI water.[55]

Electrocatalyst synthesis

To synthesize 1Ce/NGr, the Ce precursor (2.4×10^{-3} g) was introduced into 20 mL of an aqueous solution containing DCDA (1 g) and glucose (1 g) along with 3 mL of SiO_2. The mixture was sonicated for 1 h to obtain a uniform solution. Subsequently, the resulting solution was freeze-dried for 50 h to completely evaporate water and then pyrolyzed in argon at 900 °C for 2 h to obtain black Ce/NGr. After pyrolysis, the silica support was dissolved using 1.25 M of the sodium hydroxide solution, leaving behind a porous carbon network with active Ce sites (Ce/NGr). Afterward, 3Ce/NGr was obtained using the abovementioned process, but the Ce precursor amount was changed to 7×10^{-3} g. Free-standing NGr was also synthesized without the addition of the Ce precursor using the abovementioned process.[29,56,57]

Characterization

The morphological and elemental distributions of the prepared electrocatalysts were observed using FE-SEM (SU5000, Hitachi) at an operating voltage of 15.0 kV. High-resolution TEM (JEOL, JEM-2010) at an accelerating voltage of 200 kV and a mono- and double aberration-corrected transmission electron microscope (Cs TEM: SE103) were used to further analyze the catalyst morphology. The samples were dropped onto a Holey carbon-coated copper grid for the TEM analysis and then dried at 80 °C overnight. The crystal structure of the materials deposited on the working electrode was analyzed using XRD (D/Max 2005, Rigaku) with CuK_α radiation (λ = 1.54178 Å). The Raman spectra of the samples were recorded with a LabRAM ARAMIS IR2 spectrometer using a 532 nm laser device. XPS was performed with a MultiLab 2000 instrument (Thermo Fisher Scientific) using monochromated Al Kα radiation ($h\nu$ = 1486.6 eV) to investigate the surface chemical states of the elements present in the synthesized electrocatalysts. The calibration was performed based on the binding energies of the resulting C 1s peak at ~285 eV.

Conflicts of interest

There are no conflicts to declare.

Acknowledgements

This research was supported by the Nano & Material Technology Development Program through the National Research Foundation of Korea (NRF), funded by the Ministry of Science and ICT (2022M3H4A3A01082883).

References

1 D. Van Dao, T. T. D. Nguyen, T. D. Le, S.-H. Kim, J.-K. Yang, I.-H. Lee and Y.-T. Yu, *J. Mater. Chem. A*, 2020, **8**, 7687–7694.
2 S. Wang, A. Lu and C. J. Zhong, *Nano Convergence*, 2021, **8**, 4.
3 D. M. F. Santos, *et al.*, *J. Electrochem.*, 2014, **161**, F386.
4 N. Mahmood, Y. Yao, J.-W. Zhang, L. Pan, X. Zhang and J.-J. Zou, *Adv. Sci.*, 2018, **5**, 1700464.
5 B. Yang, H. Yu, X. Jia, Q. Cheng, Y. Ren, B. He and Z. Xiang, *ACS Appl. Mater. Interfaces*, 2023, **15**, 23316–23327.
6 C. Hu, J. Hu, Z. Zhu, Y. Lu, S. Chu, T. Ma, Y. Zhang and H. Huang, *Angew. Chem., Int. Ed.*, 2022, **61**, e202212397.
7 L. Cui, K. Fan, L. Zong, F. Lu, M. Zhou, B. Li, L. Zhang, L. Feng, X. Li, Y. Chen and L. Wang, *Energy Storage Mater.*, 2022, **44**, 469–476.
8 Z. Xiao, P. Sun, Z. Qiao, K. Qiao, H. Xu, S. Wang and D. Cao, *J. Chem. Eng.*, 2022, **446**, 137112.
9 Z. Bi, Y. Wang, J. Chen, X. Zhang, S. Zhou, X. Wang, T. WÅgberg and G. Hu, *Colloid Interface Sci. Commun.*, 2022, **49**, 100634.
10 H. Fu, Q. Wen, P.-Y. Li, Z.-Y. Wang, Z.-J. He, C. Yan, J. Mao, K. Dai, X.-H. Zhang and J.-C. Zheng, *Small Methods*, 2022, **6**, 2201025.
11 L. Yin, S. Zhang, M. Sun, S. Wang, B. Huang and Y. Du, *Adv. Mater.*, 2023, **35**, 2302485.
12 T. Montini, M. Melchionna, M. Monai and P. Fornasiero, *Chem. Rev.*, 2016, **116**, 5987–6041.
13 M. Melchionna and P. Fornasiero, *Mater. Today*, 2014, **17**, 349–357.
14 J. Liu, G. Li, C. Xu, H. Chen, R. Jin, L. Sun, C. Shu, H. Chen, C. Guo, H. Li and Y. Si, *Inorg. Chem. Front.*, 2023, **10**, 3091–3102.
15 S. Jiang, R. Zhang, H. Liu, Y. Rao, Y. Yu, S. Chen, Q. Yue, Y. Zhang and Y. Kang, *J. Am. Chem. Soc.*, 2020, **142**, 6461–6466.
16 Y. Jiao, Y. Zheng, M. Jaroniec and S. Z. Qiao, *Chem. Soc. Rev.*, 2015, **44**, 2060–2086.
17 H. Jin, C. Guo, X. Liu, J. Liu, A. Vasileff, Y. Jiao, Y. Zheng and S. Z. Qiao, *Chem. Rev.*, 2018, **118**, 6337–6408.
18 Y. Zhu, Q. Lin, Y. Zhong, H. A. Tahini, Z. Shao and H. Wang, *Energy Environ. Sci.*, 2020, **13**, 3361–3392.
19 J. Yu, X. Du, H. Liu, C. Qiu, R. Yu, S. Li, J. Ren and S. Yang, *Energy Fuels*, 2021, **35**, 19000–19011.
20 J. Li, Z. Zhao, Y. Ma and Y. Qu, *ChemCatChem*, 2017, **9**, 1554.
21 M. Nemiwal, T. C. Zhang and D. Kumar, *Int. J. Hydrogen*, 2021, **46**, 21401–21418.
22 R. Ikram, B. Mohamed Jan, S. Atif Pervez, V. M. Papadakis, W. Ahmad, R. Bushra, G. Kenanakis and M. Rana, *Crystals*, 2020, **10**, 1080.
23 K. Parvez, S. Yang, Y. Hernandez, A. Winter, A. Turchanin, X. Feng and K. Müllen, *ACS Nano*, 2012, **6**, 9541–9550.
24 Y. Liao, Y. Gao, S. Zhu, J. Zheng, Z. Chen, C. Yin, X. Lou and Di Zhang, *ACS Appl. Mater. Interfaces*, 2015, **7**, 19619–19625.
25 L. K. Putri, W.-J. Ong, W. S. Chang and S.-P. Chai, *Appl. Surf. Sci.*, 2015, **358**, 2–14.
26 H. Xu, L. Ma and Z. Jin, *J. Energy Chem.*, 2018, **27**, 146–160.
27 J. Zhang, Q. Zhang and X. Feng, *Adv. Mater.*, 2019, **31**, 1808167.
28 S. Hou, X. Cai, H. Wu, X. Yu, M. Peng, K. Yan and D. Zou, *Energy Environ. Sci.*, 2013, **6**, 3356–3362.
29 D. V. Dao, L. A. Cipriano, G. D. Liberto, T. T. D. Nguyen, S.-W. Ki, H. Son, G.-C. Kim, K. H. Lee, J.-K. Yang, Y.-T. Yu, G. Pacchioni and I.-H. Lee, *J. Mater. Chem. A*, 2021, **9**, 23732.
30 M. Zhu, C. Zhao, X. Liu, X. Wang, F. Zhou, J. Wang, Y. Hu, Y. Zhao, T. Yao, L.-M. Yang and Y. Wu, *ACS Catal.*, 2021, **11**, 3923–3929.
31 H.-J. Peng, G.-X. Hao, Z.-H. Chu, Y.-W. Lin, X.-M. Lin and Y.-P. Cai, *RSC Adv.*, 2017, **7**, 34104–34109.
32 M. Coros, C. Varodi, F. Pogacean, E. Gal and S. M. Pruneanu, *Sensors*, 2020, **20**, 1815.
33 U. Sim, T.-Y. Yang, J. Moon, J. An, J. Hwang, J.-H. Seo, J. Lee, K. Y. Kim, J. Lee, S. Han, B. H. Hong and K. T. Nam, *Energy Environ. Sci.*, 2013, **6**, 3658–3664.
34 Z. Bi, Y. Wang, J. Chen, X. Zhang, S. Zhou, X. Wang, T. WÅgberg and G. Hu, *Colloid Interface Sci. Commun.*, 2022, **49**, 100634.
35 Y. Zhang, Z. Sun, H. Wang, Y. Wang, M. Liang and S. Xue, *RSC Adv.*, 2015, **5**, 10430–10439.
36 V. Dao, L. A. Cipriano, S.-W. Ki, S. Yadav, W. Wang, G. Di Liberto, K. Chen, H. Son, J.-K. Yang, G. Pacchioni and I.-H. Lee, *Appl. Catal., B*, 2023, **330**, 122586.

37 M. Figueras, I. J. Villar-Garcia, F. Viñes, C. Sousa, V. A. de la Peña O'Shea and F. Illas, *J. Phys. Chem. C*, 2019, **123**, 11319–11327.
38 J. Wu, L. Ma, R. M. Yadav, Y. Yang, X. Zhang, R. Vajtai, J. Lou and P. M. Ajayan, *ACS Appl. Mater. Interfaces*, 2015, **7**, 14763–14769.
39 W. Wang, S. Xue, J. Li, F. Wang, Y. Kang and Z. Lei, *J. Power Sources*, 2017, **359**, 487–493.
40 W. Zhang, X. Qin, T. Wei, Q. Liu, J. Luo and X. Liu, *J. Colloid Interface Sci.*, 2023, **638**, 650–657.
41 Y. Jiang, M. Du, G. Cheng, P. Gao, T. Dong, J. Zhou, X. Feng, Z. He, Y. Li, L. Dai, W. Meng and L. Wang, *J. Energy Chem.*, 2021, **59**, 706–714.
42 K. H. Lim and H. Kim, *Appl. Catal., B*, 2014, **158–159**, 355–360.
43 J.-C. Li, X. Qin, F. Xiao, C. Liang, M. Xu, Y. Meng, E. Sarnello, L. Fang, T. Li, S. Ding, Z. Lyu, S. Zhu, X. Pan, P.-X. Hou, C. Liu, Y. Lin and M. Shao, *Nano Lett.*, 2021, **21**, 4508–4515.
44 N. Cheng, J.-C. Li, D. Liu, Y. Lin and D. Du, *Small*, 2019, **15**, 1901485.
45 S. Soni, V. S. Vats and S. Kumar, *et al.*, *J. Mater. Sci.: Mater. Electron.*, 2018, **29**, 10141–10153.
46 N. Suganthi and K. Pushpanathan, *J. Inorg. Organomet. Polym.*, 2019, **29**, 1141–1153.
47 J. Liu, Z. Jin, X. Wang, J. Ge, C. Liu and W. Xing, *Sci. China: Chem.*, 2019, **62**, 669–683.
48 S. Chu, W. Chen, G. Chen, J. Huang, R. Zhang, C. Song, X. Wang, C. Li and K. Ostrikov, *Appl. Catal., B*, 2019, **243**, 537–545.
49 J. Yu, Z. Wang, J. Wang, W. Zhong, M. Ju, R. Cai, C. Qiu, X. Long and S. H. Yang, *ChemSusChem*, 2020, **13**, 5273–5279.
50 Q. Li, L. Song, Z. Liang, M. Sun, T. Wu, B. Huang, F. Luo, Y. Du and C.-H. Yan, *Adv. Energy Sustainability Res.*, 2021, **2**, 2000063.
51 P. Wang, Y. Luo and G. Zhang, *et al.*, *Nano-Micro Lett.*, 2022, **14**, 120.
52 Y. Gao, T. Xiong, Y. Li, Y. Huang, Y. Li and M.-Sadeeq Jie Tang Balogun, *ACS Omega*, 2019, **4**, 16130–16138.
53 C. Zhang, Y. Shi, Y. Yu, Y. Du and B. Zhang, *ACS Catal.*, 2018, **8**, 8077–8083.
54 B. Seo, G. Y. Jung, Y. J. Sa, H. Y. Jeong, J. Y. Cheon, J. H. Lee, H. Y. Kim, J. C. Kim, H. S. Shin, S. K. Kwak and S. H. Joo, *ACS Nano*, 2015, **9**, 3728–3739.
55 M. Lismont, C. A. Páez and L. Dreesen, *J. Colloid Interface Sci.*, 2015, **447**, 40–49.
56 H. Yang, L. Shang and Q. Zhang, *et al.*, *Nat. Commun.*, 2019, **10**, 4585.
57 T. Ahmad, S. Liu and M. Sajid, *et al.*, *Nano Res.*, 2022, **1**, e9120021.